Geophysical Research Letters

Supporting Information for

Simulating the Solar Wind-Magnetosphere Interaction During the Matuyama-Brunhes Paleomagnetic Reversal

Fan Gong[1,2], Yiqun Yu[1,2*], Jinbin Cao[1,2*], Yong Wei[3*], Jiawei Gao[3], Hui Li[4], Binzheng Zhang[5], Aaron Ridley[6]

[1] School of Space and Environment, Beihang University, Beijing, China
[2] Key Laboratory of Space Environment Monitoring and Information Processing, Ministry of Industry and Information Technology, Beijing, China
[3] Institute of Geology and Geophysics, Chinese Academy of Sciences, Beijing, China
[4] State Key Laboratory of Space Weather, National Space Science Center, Chinese Academy of Sciences, Beijing, China
[5] Department of Earth Sciences, the University of Hong Kong, Hong Kong, China
[6] Department of Climate and Space Sciences and Engineering, University of Michigan, Ann Arbor, MI, USA

Contents of this file

Introduction

We provide the spherical harmonic Gauss coefficient for the intrinsic geomagnetic field during the Matuyama-Brunhes (M-B) reversal and the calculated geomagnetic power spectrum diagram of the different components of the geomagnetic field during the paleomagnetic polarity reversal. In addition, we explain the relevant equations that this work solved in the MHD simulation and provide the solar wind and interplanetary magnetic field (IMF) driving conditions for BATS-R-US.

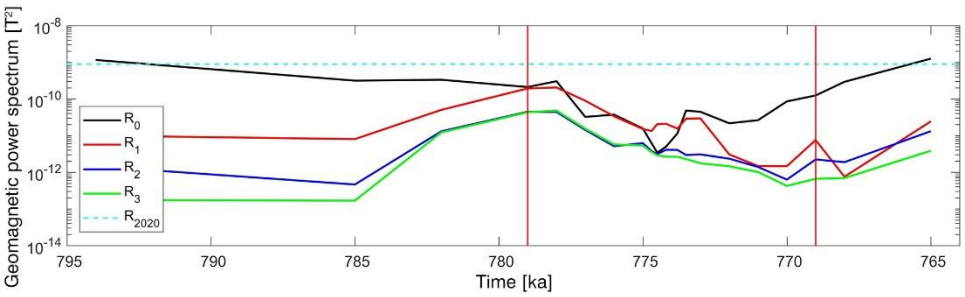

Figure S1. Geomagnetic power spectrum diagram of different components of the geomagnetic field at the Earth's surface. $\mathbf{R_0}$, $\mathbf{R_1}$, $\mathbf{R_2}$, $\mathbf{R_3}$, and $\mathbf{R_{2020}}$ represent the dipole field component, the quadrupole field component, the octupole field component, the hexadecupole field component, and the current geomagnetic field, respectively.

Text S1. The method of calculating the geomagnetic power of the different components of the geomagnetic field.

The geomagnetic field $B(r,\theta,\varphi,t)$ is produced by internal sources primarily inside Earth's core. Therefore, the geomagnetic field can be described as the gradient of a scalar potential, $B = -\nabla V$, and the potential function $V(r,\theta,\varphi,t)$ is represented as a finite series expansion in terms of spherical harmonic coefficients, g_n^m, h_n^m, also known as the Gauss coefficients:

$$V(r,\theta,\varphi,t) = a\sum_{n=1}^{N}\sum_{m=0}^{n}\left(\frac{a}{r}\right)^{n+1}[g_n^m(t)\cos m\varphi + h_n^m(t)\sin m\varphi]P_n^m(\cos\theta) \qquad (S1)$$

Here, r,θ,φ refer to coordinates in a geocentric spherical coordinate system, with r being radial distance from the center of the Earth in units of km, and θ,φ representing geocentric latitude and longitude respectively. A reference radius $a = 6371km$ s is chosen to approximate the mean Earth radius. The $P_n^m(\cos\theta)$ are Schmidt-normalized associated Legendre functions of degree n and order m (Winch et al, 2005).

Table S1 lists the spherical harmonic Gauss coefficients of the 20 moments selected for simulation during the M-B reversal in this study, which can be used with Equation (S1) to determine the geomagnetic potential (and geomagnetic field) anywhere on or above Earth's surface. In addition, we use the Mauersberger-Lowes power spectrum to calculate the mean square field of the multipole component of the paleomagnetic field (Lowes, 1966), the expression is as follows (Leonard & Fabian, 2007):

$$\mathrm{R}_n(r) = <\mathrm{B}_n(r)\cdot\mathrm{B}_n(r)> = (n+1)\left(\frac{a}{r}\right)^{2n+4}\sum_{m=0}^{n}[(g_n^m)^2 + (h_n^m)^2] \qquad (S2)$$

Figure S2 shows the geomagnetic power spectrum diagram of these different components of the geomagnetic field at the Earth's surface ($r = a = 6371km$). According to Equation (S2), R_0, R_1, R_2, and R_3 represent the dipole, quadrupole, octupole, and the hexadecupole field components respectively. The green dotted line represents the value of the current geomagnetic field. As shown in Figure S1, all these components change during the reversal period. During 779ka-774.5ka, the quadrupole component is at a comparable magnitude to the dipole component and even exceeds the dipole component briefly, which is different from a pure quadrupole field. Therefore, we expect the subsolar stand-off distance not to be as simple as from the classic Martyn-relation, although the tendency and quantitative value may be close.

g/h	n	m	794ka	785ka	782 ka	779 ka	778 ka	777 ka	776 ka	775 ka	774.7 ka	774.5 ka	774.2 ka	773.8 ka	773.5 ka	773 ka	772 ka	771 ka	770 ka	769 ka	768 ka	765 ka
g	1	0	33.67	17.72	17.77	9.66	14.43	4.21	5.97	3.31	1.57	0.70	-1.49	-3.31	-6.73	-6.55	-4.57	-5.12	-9.09	-10.91	-16.69	-35.17
g	1	1	-4.12	0.32	3.59	8.61	5.62	2.44	-0.03	-0.51	-0.63	-0.93	-0.73	0.65	1.65	1.19	-0.83	-0.10	0.29	1.47	-0.49	-1.78
h	1	1	1.75	-0.47	1.94	6.56	7.98	2.93	1.29	2.10	1.83	1.44	1.47	-0.24	0.35	0.25	-0.22	0.34	-1.61	-1.73	-3.73	-3.59
g	2	0	0.82	0.38	-0.20	-3.38	-3.66	-3.34	-1.68	-0.41	-0.75	-1.33	-1.30	-1.05	-0.79	-1.36	-0.18	0.30	0.23	-0.08	-0.07	-1.86
g	2	1	1.58	1.74	3.49	6.77	7.56	4.71	3.45	2.34	2.18	2.64	2.65	2.37	3.33	3.32	1.09	0.78	0.79	1.57	0.47	-0.03
g	2	2	-0.84	-0.55	-2.06	-4.00	-4.55	-2.27	-1.33	-0.98	-0.71	-0.68	-1.09	-0.89	-0.32	-0.80	-0.52	-0.07	0.02	-0.01	-0.02	0.15
h	2	1	-0.60	-0.72	-2.81	-4.61	-3.20	-2.40	0.32	0.63	0.88	0.94	0.70	0.46	1.64	1.09	-0.07	0.17	-0.09	-1.14	-0.34	-2.95
h	2	2	0.86	-0.09	0.84	1.36	0.87	0.60	0.30	-0.73	-0.23	-0.34	-0.34	-0.11	-0.13	-0.04	-0.19	0.11	0.20	0.13	0.19	-0.01
g	3	0	-0.31	0.04	1.27	1.79	1.89	0.79	0.56	0.84	0.64	0.42	0.27	0.16	-0.07	0.18	0.43	0.40	0.06	-0.30	-0.25	-1.09
g	3	1	0.30	0.15	-0.21	-0.26	-0.47	-0.47	-0.28	-0.62	-0.53	-0.65	-0.51	-0.20	0.17	0.07	-0.47	-0.31	0.02	0.09	0.21	-0.39
g	3	2	0.31	0.11	-0.81	-1.64	-1.63	-1.11	-0.63	-0.28	-0.27	-0.09	0.11	0.00	0.34	0.40	-0.08	-0.08	-0.12	0.12	-0.21	0.00
g	3	3	-0.12	-0.26	-1.06	-2.29	-2.57	-1.20	-0.84	-0.66	-0.54	-0.50	-0.72	-0.71	-0.52	-0.63	-0.35	-0.20	-0.13	-0.15	-0.05	0.30
h	3	1	-0.11	-0.06	-0.42	-0.42	0.09	-0.55	0.03	0.61	0.45	0.42	0.64	0.51	0.46	0.16	0.33	0.35	0.04	0.02	-0.27	-0.51
h	3	2	-0.28	-0.20	-0.50	-1.32	-0.79	-0.66	-0.12	0.18	0.04	-0.03	-0.29	-0.67	-0.49	-0.53	-0.36	-0.21	-0.37	-0.76	-0.53	-1.63
h	3	3	0.31	0.07	0.71	1.31	0.99	0.71	0.45	-0.25	0.00	-0.01	0.03	0.28	0.34	0.34	-0.01	0.01	0.19	0.17	0.35	0.22
g	4	0	-0.06	0.10	0.90	1.50	1.59	0.78	0.61	0.76	0.65	0.62	0.58	0.51	0.45	0.32	0.45	0.35	0.13	0.02	-0.05	-0.17
g	4	1	-0.10	0.13	1.07	2.16	2.29	1.31	0.74	0.57	0.44	0.36	0.24	0.14	0.13	0.24	0.08	0.02	-0.07	-0.19	-0.16	-0.55
g	4	2	0.07	-0.02	-0.50	-0.77	-0.76	-0.50	-0.17	-0.29	-0.20	-0.19	-0.11	0.01	0.17	0.14	-0.13	-0.07	0.06	0.07	0.13	-0.09
g	4	3	0.05	-0.04	-0.57	-1.33	-1.36	-0.90	-0.54	-0.31	-0.29	-0.26	-0.18	-0.23	-0.18	-0.13	-0.11	-0.05	-0.07	-0.02	-0.11	-0.13
g	4	4	0.00	-0.08	-0.31	-0.69	-0.84	-0.35	-0.30	-0.28	-0.23	-0.21	-0.28	-0.27	-0.20	-0.21	-0.15	-0.12	-0.07	-0.07	-0.02	0.18
h	4	1	0.04	-0.06	-0.47	-0.65	-0.60	-0.31	-0.06	-0.06	0.02	0.08	0.14	0.21	0.23	0.21	0.11	0.11	0.12	0.15	0.15	0.30
h	4	2	-0.06	0.01	0.06	0.04	0.28	-0.14	0.12	0.38	0.29	0.25	0.32	0.26	0.13	0.00	0.25	0.28	0.11	0.06	-0.08	-0.35
h	4	3	-0.09	0.00	0.26	0.37	0.53	0.27	0.11	0.15	0.03	-0.02	-0.14	-0.32	-0.34	-0.31	-0.18	-0.15	-0.20	-0.30	-0.26	-0.60
h	4	4	0.10	0.05	0.34	0.69	0.59	0.37	0.26	-0.01	0.07	0.07	0.10	0.20	0.24	0.23	0.03	0.01	0.08	0.07	0.14	0.07

Table S1. Spherical harmonic Gauss coefficients during M-B reversal.

ρ(cm^3)	V_x(km/s)	V_y(km/s)	V_z(km/s)	B_x(nT)	B_y(nT)	B_z(nT)	T(K)
5	400	0	0	0	0	-10	10^5

Table S2. The solar wind and IMF driving conditions.

Text S2. MHD equations for our simulations studying the solar wind-magnetosphere interactions.

Our simulation is Cartesian and solves for eight parameters in Table S2: mass density (ρ), velocity (V_x, V_y, V_z), magnetic field (B_x, B_y, B_z), and thermal pressure (P_T, given by temperature (T)). These are found through iteratively solving a set of ideal MHD equations: the mass conservation, momentum conservation, magnetic induction, and energy conservation equations, respectively:

$$\frac{\partial \rho}{\partial t} + \nabla \cdot (\rho \vec{u}) = 0 \tag{S3}$$

$$\frac{\partial (\rho \vec{u})}{\partial t} + \nabla \cdot \left[\rho \vec{u}\vec{u} + \left(P_T + \frac{B^2}{8\pi} \right) I - \frac{\vec{B}\vec{B}}{4\pi} \right] = \rho \vec{g} \tag{S4}$$

$$\frac{\partial \vec{B}}{\partial t} + \nabla \cdot \left(\vec{u}\vec{B} - \vec{B}\vec{u} \right) = 0 \tag{S5}$$

$$\frac{\partial \epsilon}{\partial t} + \nabla \cdot \left[\vec{u} \left(\epsilon + P_T + \frac{B^2}{8\pi} \right) I - \frac{(\vec{u} \cdot \vec{B})\vec{B}}{4\pi} \right] = \rho \vec{g} \cdot \vec{u} \tag{S6}$$

where I denotes the identity matrix and $\vec{g}$ the acceleration due to gravity. The total energy density ϵ is

$$\epsilon = \frac{\rho u^2}{2} + \frac{P_T}{\gamma - 1} + \frac{B^2}{8\pi} \tag{S7}$$

with $\gamma = 5/3$.

Details of the MHD model can be found in Powell et al. (1999). In this study, the simulation domain expands from $X = -224$ to $32\ Re$, $Y = -128$ to $128\ Re$, and $Z = -128$ to $128\ Re$. With the upstream solar wind driving conditions, as listed in Table S2, specified at $X = 32\ Re$, the MHD model runs iteratively for 100,0000 steps.